energies

Article

Modeling, Analysis, Design, and Simulation of a Bidirectional DC-DC Converter with Integrated Snow Removal Functionality for Solar PV Electric Vehicle Charger Applications

Sandra Aragon-Aviles, Arvind H. Kadam, Tarlochan Sidhu * and Sheldon S. Williamson

Department of Electrical, Computer and Software Engineering, Faculty of Engineering and Applied Sciences, Ontario Tech University, Oshawa, ON L1G 0C5, Canada; sandra.aragonaviles@ontariotechu.net (S.A.-A.); arvind.kadam@ontariotechu.net (A.H.K.); sheldon.williamson@ontariotechu.ca (S.S.W.)

* Correspondence: tarlochan.sidhu@ontariotechu.ca

Abstract: Different factors affect solar photovoltaic (PV) systems by decreasing input energy and reducing the conversion efficiency of the system. One of these factors is the effect of snow cover on PV panels, a subject lacking sufficient academic research. This paper reviews and compares current research for snow removal in solar PV modules. Additionally, this paper presents the design, analysis and modelling of a smart heating system for solar PV Electric Vehicle (EV) charging applications. The system is based on a bidirectional DC-DC converter that redirects the grid/EV-battery power into heating of the solar PV modules, thus removing snow cover, as well as providing the function of MPPT when required to charge the EV battery pack. A control scheme for each mode of operation was designed. Subsequently, a performance evaluation by simulating the system under various conditions is presented validating the usefulness of the proposed converter to be used in solar PV systems under extreme winter conditions.

Keywords: bidirectional converter; DC-DC converter; EV charging; solar PV system; synchronous buck converter

check for updates

Citation: Aragon-Aviles, S.; Kadam, A.H.; Sidhu, T.; Williamson, S.S. Modeling, Analysis, Design, and Simulation of a Bidirectional DC-DC Converter with Integrated Snow Removal Functionality for Solar PV Electric Vehicle Charger Applications. *Energies* **2022**, *15*, 2961. https://doi.org/10.3390/en15082961

Academic Editors: Armita Hamidi and Sarvenaz Sobhansarbandi

Received: 5 January 2022
Accepted: 6 April 2022
Published: 18 April 2022

1. Introduction

Different studies have revealed the potential of various renewable energy sources to be utilized for human energy consumption in the world; among all the energies, solar energy is the most promising due to its high potential (3,850,000 EJ) [1]. Despite its huge potential, the production of solar energy to contribute to the power supply demand is not significant [1,2]. At the same time, there are different limitations in solar PV systems that have made their implementation slow since their appearance. Some of the limitations of solar PV systems include price (the relation between lifetime generation cost versus electricity prices), energy storage, efficiency, among others.

According to Ueda et al. [3] the efficiency of solar PV systems can be affected by meteorological parameters that decrease the input energy such as shading, soiling, snow covering, mismatch, etc.; or parameters that reduce the conversion efficiency such as module temperature, losses, equipment efficiency, and others [3].

Most of these factors have been researched in-depth, such as the effects of shading and mismatch or the efficiency of the converters used, resulting in an improvement in system efficiency [4–10]. The current converters developed have an efficiency of around 90% or higher; however, more research is still required to improve the input energy efficiency of solar PV cells [11–14]. Many studies have been developed on the effects of snowfall on solar PV systems since this is one of the main factors affecting the performance of PV systems in cold areas [10,15–32].

Several active and passive heating systems for snow removal of PV modules have been proposed in the literature. In Canada, the company Soltek Solar Energy Ltd. (Victoria, BC, Canada) developed flush mount panels to reduce the snow covering issue on solar modules, however, there are still problems of icing on the modules [33]. Also, the use of different self-cleaning surfaces for solar modules has been commercially developed, such as hydrophilic and superhydrophobic surfaces, which are made to repel water by forming beads of water that roll across the surface. There have also been attempts to create icephobic surface coatings, which repel ice or inhibit ice formation [20,27,30,32,33]. However, there are no conclusive and effective results related to these materials.

Ross and Usher [33,34] proposed a heating system that melts snow using reflected radiation from the ground to heat the back surface of the PV module by using a black absorbent coating placed on the back of the module mounted alongside with a glass enclosure, although the results found were negligible.

Various patents were developed in Germany, Japan, and Sweden [35–37], with all of them using the same active method, but using a different type of sensors for the control system. The proposed system consisted of applying a reverse current to the solar panel using an external power source in order to heat the solar cells, thus melting the snow. This method essentially used the heating phenomenon of the forward biased diodes of the solar PV panel once they start conducting the current. Therefore, when the solar panels are covered with snow, if a forward bias voltage approximately equal to or greater than its built-in voltage is applied, it will start conduction in the forward direction of the diode, which will eventually dissipate some of the power as heat, increasing the temperature of the solar panels and, consequently, melting the layer of snow/ice adhering to their tilted surfaces [38]. Other methods included the use of resistive electrical cables to heat the frame of the PV modules that would produce an avalanche effect to remove snow. Several studies using these methods were found in the literature [37–42]. However, although they have had good results in reducing the losses in the system caused by the snow cover, most of these systems have used many sensors, such as photodetectors, temperature sensors and pyranometers, and also lack relevant historical data to draw decisive conclusions.

In this work, a bidirectional DC-DC buck-boost converter capable of extracting the maximum power point (MPPT) of a solar PV array to charge an EV battery pack is proposed. The proposed system, in addition to allowing a direct current flow to the EV battery, is also designed to provide a reverse current flow to heat the solar cells of the solar PV array, which is the main contribution of this work. This feature will allow to melt the snow in severe winter conditions, thereby improving the annual efficiency of any off-grid or on-grid PV EV charger system. Unlike systems found in the literature, this approach proposes the use of power from the EV battery pack or from the grid to provide the current needed to heat the solar cells, rather than using external power sources. Furthermore, although this work only focuses on analysis, design and simulation, it is important to mention that for its implementation, this system does not require sensors to detect the snow cover on the solar panels; this can be implemented by getting the weather forecast of the location where the system is installed by using a location-based algorithm developed in the Python programming language. In this way, the heating system will be activated when there is a snow alert in the area.

For analysis and design purposes, the solar PV array was modeled using a Norton equivalent circuit and a single-diode model to be able to control the system in the boost mode of operation. However, for the buck mode of operation, this same solar PV array was modeled as a resistive load.

All the analyses are explained in detail in the sections below as follows: Section 2 includes the analysis, design and modeling of the proposed converter and its controller, starting from a very detailed analysis of the characteristics of the solar PV modules, continuing with the design and modeling of the converter and ending with the design of the controller in the different modes of operation; in Section 3, the simulation results obtained from the validation test of the proposed control are explained and, finally, in Section 4, the conclusions of this work are summarized.

2. Design, Analysis and Modelling of the Proposed System

The main focus of this article is the modeling, analysis and design of a bidirectional DC-DC converter with MPPT and snow removal functionality, which will allow the power transfer to charge the EV battery pack and a reverse flow of current to produce heat on the solar cells that will melt the snow over the solar panels in winter time.

2.1. Photovoltaic Design Considerations

In this study, Trina Solar panels, namely model TSM-245-PA05 (245 W) were used. These solar panels were provided by the company "Upstartz Energy Ltd." (Oshawa, ON, Canada) who participated as a sponsor in this study. The characteristics of the solar panel are shown in Table 1.

Table 1. Solar panel characteristics.

Parameter	Specifications
Module Model	Trina Solar TSM-245-PA05
Solar Cells Type	Multicrystalline
Peak Power (P_{MAX})	245 Wp
Power Output Tolerance	±3%
Open Circuit Voltage (V_{OC})	37.5 V *
Short Circuit Current (I_{SC})	8.68 A *
Maximum Power Voltage (V_{MP})	30.2 V *
Maximum Power Current (I_{MP})	8.13 A *
Temperature Coefficient of P_{MAX}	−0.43%/°C
Temperature Coefficient of V_{OC}	−0.32%/°C
Temperature Coefficient of I_{SC}	0.047%/°C
Module Efficiency (η m)	15%
Module Dimensions	1650 × 992 × 35 mm

* Values at Standard Test Conditions STC (Air Mass AM1.5, irradiance 1000 W/m^2, Cell Temperature 25 °C).

The maximum dimensions of a parking space (6.0 m by 3.2 m) in Ontario, Canada, were considered, giving an approximate area of 19 m^2. The system proposed is a compound of an array of 9 solar PV panels connected in series. The I-V and P-V characteristic curves of the solar PV array for different irradiance levels are presented in Figure 1a,b respectively. The irradiance for each condition shown goes from 0 kW/m^2 to 1 kW/m^2.

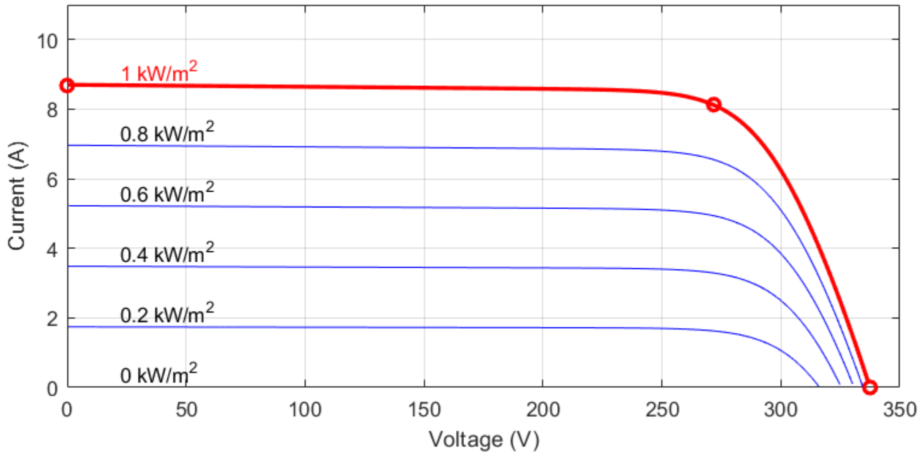

(a)

Figure 1. *Cont.*

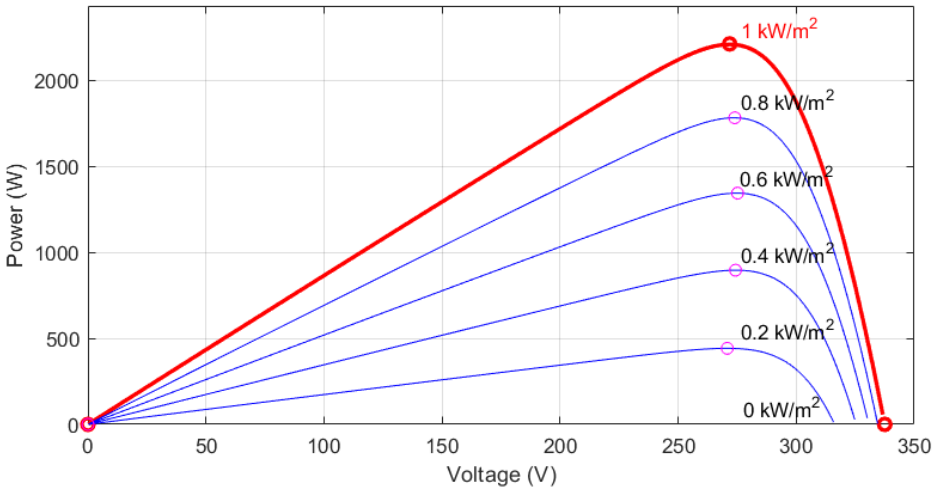

(**b**)

Figure 1. Characteristic curves of PV array of 9 solar PV modules series connected (model TSM-245-PA05): (**a**) Solar PV array I-V curve; (**b**) Solar PV array P-V curve.

From the above figure, it can be seen that at an irradiance of 1 kW/m^2, the MPP is found at 2209.73 W, with a voltage at the MPP of 271.8 V and a current at the MPP of 8.13 A.

Using the main specifications of the solar panel mentioned in Table 1, the solar PV array can be modeled using a non-linear and a linear model applying the methodology of Dr. Ramos-Paja in [43,44].

The values of the equation of the single-diode simplified model were identified by using the curve fitting tool of MATLAB. The model is shown in Figure 2. Then, the non-linear model of the solar PV array can be expressed as:

$$I_{pv} = I_{sc} - A \cdot e^{B \cdot V_{pv}} = 8.68 - 6.076 \times 10^{-6} \cdot e^{0.04199 \cdot V_{pv}} \tag{1}$$

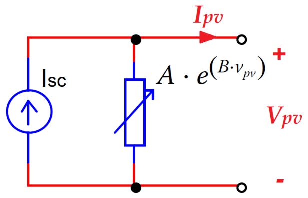

Figure 2. Simplified single-diode model of a solar PV array.

However, this model can only be used for electrical simulation purposes and not for control design. Therefore, a Norton equivalent circuit was calculated when the solar PV array is under standard conditions (irradiance equal to 1000 W/m^2 and ambient temperature equal to 25 °C), obtaining the equivalent resistance R_{pv} as a result:

$$R_{pv} = \frac{V_{pv}}{I_{sc} - I_{pv}} = \frac{271.8}{8.68 - 8.13}\ \Omega = 494.1818\ \Omega \tag{2}$$

The Norton equivalent model is shown in Figure 3.

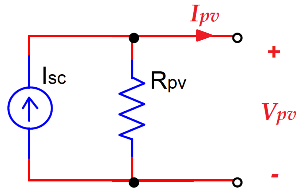

Figure 3. Norton equivalent model of a solar PV array.

A comparison between the non-linear model and the linear model (Norton equivalent) of a solar PV array at its MPP under standard conditions is shown in Figure 4. The single-diode simplified model is represented by the red line and the Norton model is represented by the blue line.

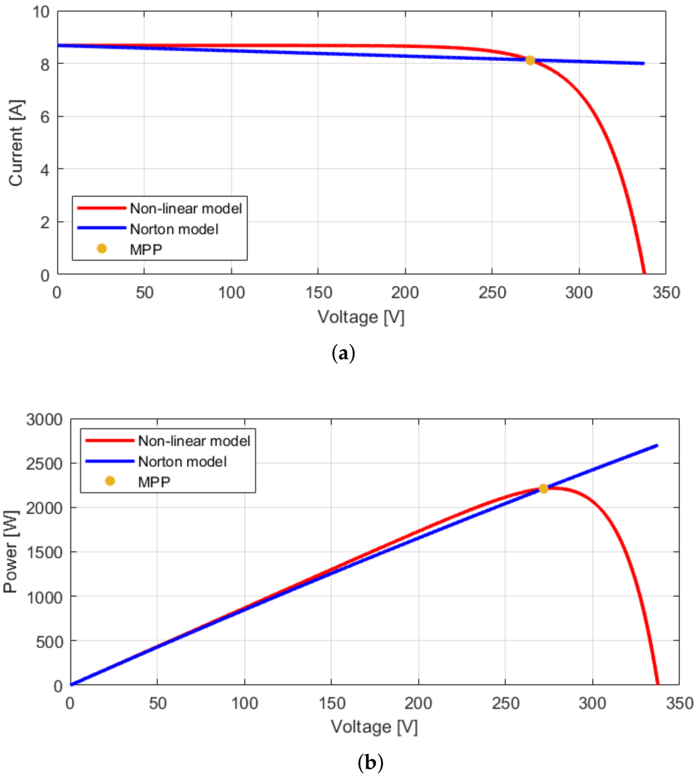

Figure 4. Comparison of I-V and P-V characteristic curves for the non-linear and linear models of the solar PV array calculated: (**a**) I-V Characteristic curve. (**b**) P-V characteristic curve.

From Figure 4, it can be concluded that the Norton model is a very accurate representation of the non-linear model in the MPP and very close for values lower than the MPP. Therefore, this model can be used for simulation and control design purposes.

2.2. Proposed Power Conversion Topology

A controlled bidirectional buck-boost DC-DC converter, also known as bidirectional half-bridge converter (BHBC) or synchronous buck converter (SBC), has been chosen to be used for this application. A non-isolated topology was chosen because it is cheaper than the isolated topologies, and has fewer components. Apart from that, the SBC has the advantage of keeping the same electrical reference for the input and output ports [45]. However, its main drawbacks are the pulsating current in the higher voltage port and the lack of insulation [45]. Figure 5 shows the overall structure of the solar PV system with snow removal functionality for off-grid and grid-connected EV charger applications.

In order to prove the concept of functionality of the proposed bidirectional converter, it will be assumed that the voltage at the DC bus where the EV battery pack is connected will be regulated by either the bidirectional AC-DC converter in the case of the grid-connected system; or by the bidirectional DC-DC converter that interconnects the battery pack and the main battery in the case of the off-grid system. Hence, the main battery/grid will serve as a power source to supply the reverse current flow necessary to heat the solar cells of the solar PV array, performing the snow removal functionality of the system when necessary.

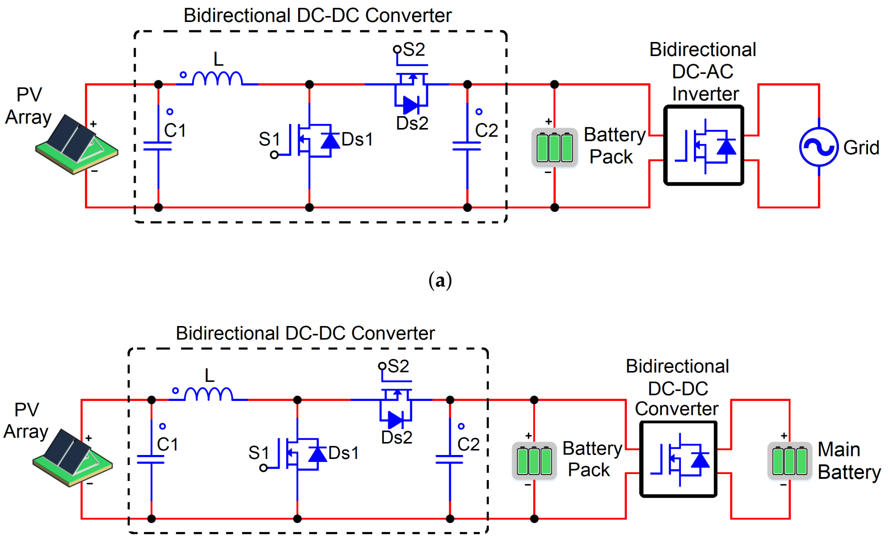

(**a**)

(**b**)

Figure 5. Overall structure of the solar PV system with snow removal functionality for off-grid and grid-connected EV charger applications: (**a**) Grid-connected. (**b**) Off-grid.

Although both systems showed above, i.e., grid-connected and off-grid, are composed of two bidirectional converters, this article only focuses on the analysis, design and modeling of the proposed bidirectional buck-boost DC-DC converter that interconnects the solar PV array and the battery pack.

2.3. Modes of Operation of the Proposed Bidirectional DC-DC Converter

Figure 6 depicts the circuit diagram of the bidirectional buck-boost DC-DC converter. This converter interfaces the solar PV array and the EV battery pack. Depending on the operating scenario, two modes of operation can be set: boost and buck mode. The converter operates with two controllable switches (S_1, S_2); the operation of the two switches is complementary, meaning that when one is ON the other must be OFF.

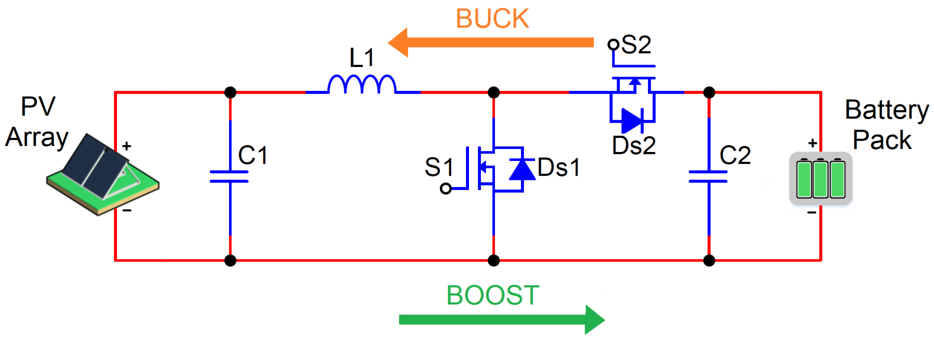

Figure 6. Modes of operation of the proposed converter (Boost + Buck).

Depending on the maximum duty cycle, it will operate in boost mode when switch S_1 is triggered, while buck mode will operate when switch S_2 is triggered. An inductor L_1 at the input provides a non-pulsating current and can have a direct power transfer from source to load (EV battery pack). It is important to consider preventing the simultaneous conduction of both switches. The controller must ensure that both switches are not turned on simultaneously as this would place a very small parasitic resistance between the input and ground and destructive currents could flow through the switches. It must be ensured that there is a dead time in which both switches are off [46].

2.4. Design of Bidirectional DC-DC Converter

The following section provides detailed descriptions of the component design of the proposed bidirectional buck-boost converter that guarantees operation in any mode of operation. However, before going into details, the following assumptions will be considered during the analysis:

- All the components are considered ideal; ON period forward voltage drops and equivalent series resistance (ESR) of the components are neglected;
- The selection of the inductor (L_1) is such that the converter always operates in continuous conduction mode (CCM);
- The output voltage ripple is negligible;
- In steady state operation, both the integral of Volts-sec through an inductor, as well as the integral of Amp-sec through a capacitor, during one cycle will be equal to zero.

Figure 7 depicts the framework of the bidirectional buck-boost DC-DC converter proposed for the snow removal and charging application.

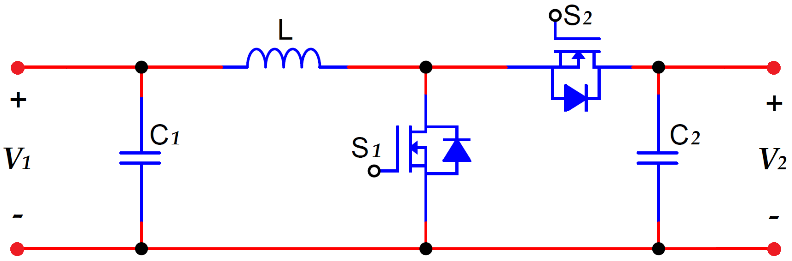

Figure 7. Framework of the bidirectional buck-boost DC-DC converter.

The following design requirements are used to calculate the components of the proposed converter:

- PV panel string peak power: 2.2 kW;
- PV panel voltage range: 225 to 320 V_{dc} (considering 17% of losses due to heating of the solar panels at 65 °C and change in the irradiance);
- Nominal battery voltage range: 320 to 400 V_{dc};
- Maximum output current: 5.5 A;
- Switching frequency: 30 kHz.

Using the equations given by [47,48] when the DC-DC converter works in the Boost CCM, the components can be designed as follows:

Duty cycle for minimum input voltage, where the efficiency estimated of the converter is 95%:

$$D = 1 - \frac{V_{1(min)}\eta}{V_2} = 1 - \frac{225 \times 0.95}{400} = 0.4656 \tag{3}$$

Inductor ripple current estimation, considering the inductor ripple current as 20% of output current:

$$\Delta I_L = \frac{(0.2 I_{2(max)})V_2}{V_1} = \frac{(0.2 \times 5.5)400}{225}\,\text{A} = 1.9555\ \text{A} \tag{4}$$

Then, the inductor calculation will be as follows:

$$L = \frac{V_1(V_2 - V_1)}{\Delta I_L f_s V_2} = \frac{225(400 - 225)}{1.955 \times 30 \times 10^3 \times 400}\,\text{H} = 1677.91\ \mu\text{H} \tag{5}$$

A higher inductance was selected to keep the current ripple in the range. The value selected is 2100 μH.

Then, the minimum output capacitance estimating an output voltage variation of 1% was calculated:

$$C_2 = \frac{I_{2(max)}D}{\Delta V_2 f_s} = \frac{5.5 \times 0.4656}{(0.01 \times 400)(30 \times 10^3)}\ \mathrm{F} = 21.34\ \mu\mathrm{F} \tag{6}$$

A higher capacitance was selected to keep the voltage ripple in the range. The value selected is 27 μF.

Using the equations given by [47,49], when the DC-DC converter works in the Buck CCM, the maximum duty cycle with an estimated efficiency of 95% can be expressed as:

$$D = \frac{V_1}{V_2\eta} = \frac{320}{400 \times 0.95} = 0.9421 \tag{7}$$

Then, the minimum input capacitance estimating an input voltage variation of 1%, in the Buck CCM is calculated:

$$C_1 = \frac{V_2 D(1-D)}{8 f_s^2 L \Delta V_1} = \frac{400 \times 0.9421(1-0.9421)}{8(30 \times 10^3)(2.1 \times 10^{-3})(0.01 \times 225)}\ \mathrm{F} = 1.56\ \mu\mathrm{F} \tag{8}$$

A higher capacitance was selected to keep the voltage ripple in the range. The value selected is 2 μF. A summary of the parameter values is shown in Table 2.

Table 2. Parameters of the system.

Parameter	Value
Input Voltage Range ($V_{1(Min)}$–$V_{1(Max)}$)	225–320 V
PV Voltage at MPP (V_1)	271.8 V
Output Voltage (V_2)	400 V
Maximum Input Current ($I_{1(Max)}$)	8.13 A
Maximum Output Current ($I_{2(Max)}$)	5.5 A
Power Rating	2.2 kW
Efficiency (η)	95%
Inductance (L)	2100 μH
Output Capacitance (C_2)	27 μF
Input Capacitance (C_1)	2 μF
Switching Frequency (f_s)	30 kHz
Output and Input Voltage Variation	1 %

2.5. Mathematical Modeling

The following section provides in-depth descriptions regarding the mathematical modelling of the proposed bidirectional buck-boost converter operating under boost and buck mode.

2.5.1. Buck Operation Mode

In this mode of operation, the converter is regulating the solar PV array (input port). It is assumed that an additional converter as the one shown in Figure 5 is regulating the voltage of the EV battery pack and at the same time supplying the required power to be transferred to the solar PV array in order to heat the PV cells. Figure 8 depicts the converter circuit operating in buck mode, where the solar PV array is represented by a load R_{PV} and the DC bus/EV battery pack is represented by a voltage source V_{bus}. Capacitance C_2 is not included in the circuit because it has no dynamic effect when the output port has a regulated voltage. The mathematical modelling was obtained by using the methodology applied by [44,50].

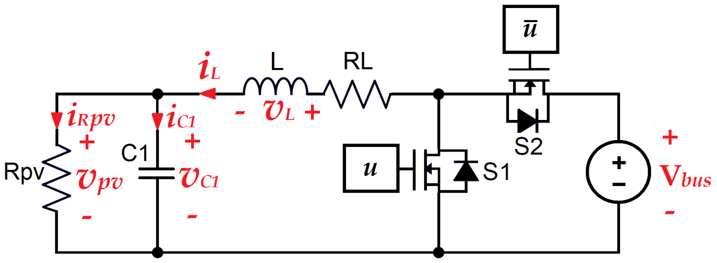

Figure 8. Circuit diagram of the bidirectional buck-boost DC-DC converter operating in Buck mode.

Applying the state-space averaging method, the following dynamic model and equilibrium points are obtained:

$$I_L = I_{PV}; \quad V_{C1} = I_{PV}R_{PV}; \quad D = 1 - I_{PV}\left(\frac{R_{PV}+R_L}{V_{bus}}\right) \tag{9}$$

$$L\frac{d\tilde{i}_L(t)}{dt} = \underbrace{V_{bus}(1-D) - I_L\alpha - V_{C1}\beta}_{\text{Equilibrium point}} + \underbrace{\tilde{v}_{bus}(1-D) - \tilde{i}_L\alpha - \tilde{v}_{C1}\beta - \tilde{d}v_{bus}}_{\text{Linear}} - \underbrace{\tilde{v}_{bus}\tilde{d}}_{\text{Non-linear}} \tag{10}$$

$$C_1\frac{dv_{C1}(t)}{dt} = \underbrace{I_L R_{PV}\gamma - V_{C1}\gamma}_{\text{Equilibrium point}} + \underbrace{\tilde{i}_L R_{PV}\gamma - \tilde{v}_{C1}\gamma}_{\text{Linear}} \tag{11}$$

where:

$$\left.\begin{aligned} \alpha &= R_L + \frac{R_{PV}R_{C1}}{R_{PV}+R_{C1}} \\ \beta &= 1 - \frac{R_{C1}}{R_{PV}+R_{C1}} \\ \gamma &= \frac{1}{R_{PV}+R_{C1}} \end{aligned}\right\} \tag{12}$$

In the above equations, three components of the model can be identified: the equilibrium point which contains DC terms; the linear dynamic component which includes the first order AC terms; and the non-linear dynamic component which includes the second order AC terms [51].

By applying the Laplace transform to the linear part of (10) and (11), and omitting the disturbances, the following transfer functions are obtained for the dynamic variables of the converter in relation to the duty cycle:

$$G_{id}(s) = \frac{I_L(s)}{D(s)} = \frac{\dfrac{-V_{bus}(C_1 s + \gamma)}{LC_1}}{s^2 + \dfrac{(L\gamma + C_1\alpha)}{LC_1}s + \dfrac{R_{PV}\gamma\beta}{LC_1}} \tag{13}$$

$$G_{vd}(s) = \frac{V_{C1}(s)}{D(s)} = \frac{\dfrac{-V_{bus}R_{PV}\gamma}{LC_1}}{s^2 + \dfrac{(L\gamma + C_1\alpha)}{LC_1}s + \dfrac{R_{PV}\gamma\beta}{LC_1}} \tag{14}$$

As can be noted in (13), $G_{id} = (I_L(s))/D(s)$ has a negative sign and the transfer function shows a non-minimum phase nature, produced by a zero located in the right-half-plane. The control objective in this mode of operation is to enforce $i_L = I_{LRef}$. By replacing all the values in the equilibrium point, the transfer function of G_{id} is obtained as follows:

$$G_{id}(s) = \frac{-1.905 \times 10^5 s - 2.846 \times 10^9}{s^2 + 1.529 \times 10^4 s + 2.428 \times 10^8} \tag{15}$$

Additionally, an AC analysis was performed using the AC sweep tool of PSIM. Both, the model and the circuit were analyzed by injecting a small AC excitation signal as perturbation into the system input signal, and the frequency responses of both were compared. The comparison of the frequency responses of the mathematical model and the circuital model for inductor current $I_L(s)$ and input capacitor voltage $V_{C1}(s)$ are shown in Figure 9. The frequency responses of the circuital model simulated in PSIM compared with the analytical small-signal model exhibits a satisfactory agreement for i_L and V_{C1} variables up to 12 kHz. According to these results it can be concluded that the adopted model accurately describes the system dynamics; therefore, it is suitable for control purposes.

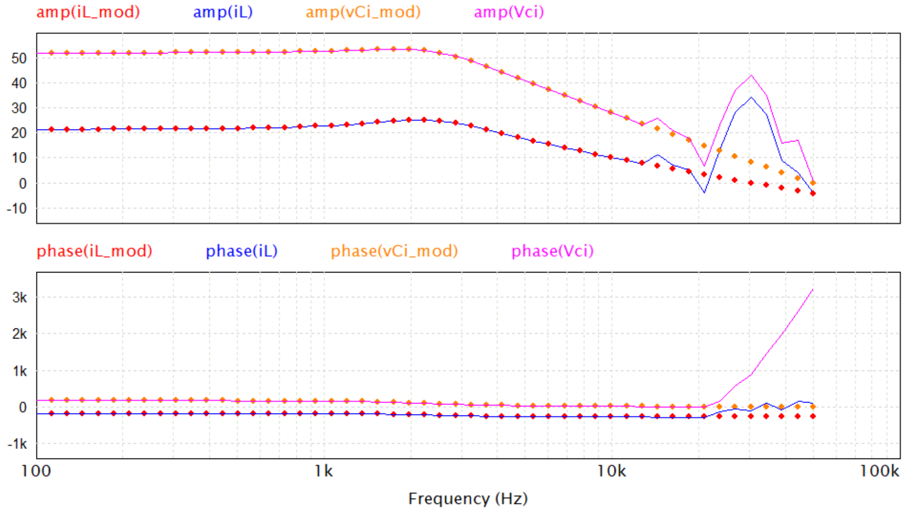

Figure 9. Comparison of the frequency responses of the linear model and the PSIM circuit in the Buck mode for inductor current $I_L(s)$ and input capacitor voltage $V_{C1}(s)$. [● and ●: mathematical model results. — and —: circuital simulation results].

2.5.2. Boost Operation Mode

In this mode of operation, the converter is fed by the solar PV array and has the function of regulating the maximum power point (MPP) provided by the solar PV array. Figure 10 depicts the converter equivalent circuit for the boost operation mode, where the EV battery pack connected at the DC bus is represented by a voltage source V_{bus} and the solar PV array is represented by the Norton equivalent model analyzed before. Again, capacitance C_2 is not included for the same reason stated in the buck mode. The mathematical modelling was found by using the methodology applied by Dr. Ramos-Paja [44,50].

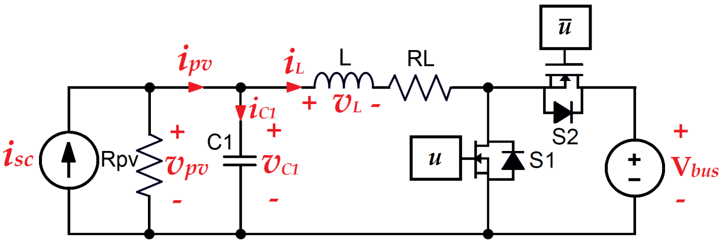

Figure 10. Circuit diagram of the bidirectional buck-boost DC-DC converter operating in the Boost mode.

Applying the same procedure as in the buck mode, the following dynamic model, and equilibrium point are obtained:

$$I_L = I_{PV} = I_{MPP}; \quad V_{C1} = V_{PV} = V_{MPP}; \quad D = 1 - \frac{V_{MPP} - I_{MPP}R_L}{V_{bus}} \tag{16}$$

$$\begin{aligned} L\frac{d\tilde{i}_L(t)}{dt} = {} & \underbrace{-V_{bus}(1-D) - I_L\alpha + V_{C1}\beta + I_{sc}R_{PV}R_{C1}\gamma}_{\text{Equilibrium point}} + \\ & \underbrace{-\tilde{v}_{bus}(1-D) - \tilde{i}_L\alpha + \tilde{v}_{C1}\beta + \tilde{i}_{sc}R_{PV}R_{C1}\gamma + \tilde{d}v_{bus}}_{\text{Linear}} + \underbrace{\tilde{v}_{bus}\tilde{d}}_{\text{Non-linear}} \end{aligned} \tag{17}$$

$$C_1\frac{dv_{C1}(t)}{dt} = \underbrace{-I_LR_{PV}\gamma - V_{C1}\gamma + I_{sc}R_{PV}\gamma}_{\text{Equilibrium point}} - \underbrace{\tilde{i}_LR_{PV}\gamma - \tilde{v}_{C1}\gamma + \tilde{i}_{sc}R_{PV}\gamma}_{\text{Linear}} \tag{18}$$

where α, β and γ are as stated before in (12).

The state space system is now characterized by the following vectors:

$$X = \begin{bmatrix} i_L \\ v_{C1} \end{bmatrix}; \quad U = \begin{bmatrix} d \\ i_{sc} \\ v_{bus} \end{bmatrix} \tag{19}$$

As well as, by the Jacobian matrices given as follows:

$$A_m = \begin{bmatrix} -\frac{\alpha}{L} & \frac{\beta}{L} \\ -\frac{R_{PV}\gamma}{C_1} & \frac{\gamma}{C_1} \end{bmatrix}; \quad B_m = \begin{bmatrix} \frac{V_{bus}}{L} & \frac{R_{PV}R_{C1}\gamma}{L} & -\frac{1-D}{L} \\ 0 & 0 & \frac{R_{PV}\gamma}{C_1} \end{bmatrix} \tag{20}$$

The system output defined is the PV voltage V_{PV}, which is expressed as follows:

$$V_{PV} = v_{c1} + i_{C1}R_{C1}\alpha \tag{21}$$

Then, matrices C_m and D_m were defined:

$$C_m = \begin{bmatrix} -R_{PV}R_{C1}\gamma & \beta \end{bmatrix}; \quad D_m = \begin{bmatrix} 0 & 0 & R_{PV}R_{C1}\gamma \end{bmatrix} \tag{22}$$

To validate the proposed model, the transfer function between the duty cycle and the PV voltage $G_{vd}(s) = V_{pv}(s)/D(s)$ was calculated using MATLAB by replacing all the values in equilibrium point on the mathematical model found:

$$G_{vd}(s) = \frac{V_{PV}(s)}{D(s)} = \frac{-6666s - 9.523 \times 10^{10}}{s^2 + 1362s + 2.384 \times 10^8} \tag{23}$$

As can be noted in (23), G_{vd} has the same characteristics as the transfer function found in the buck mode analysis. The control objective in this mode of operation is to enforce $v_{pv} = V_{pvRef}$.

An AC analysis was performed using the AC sweep tool of PSIM as in the previous analysis for the buck mode. The comparison of the frequency responses of the mathematical model and the circuital model for solar PV array voltage $V_{pv}(s)$ are shown in Figure 11.

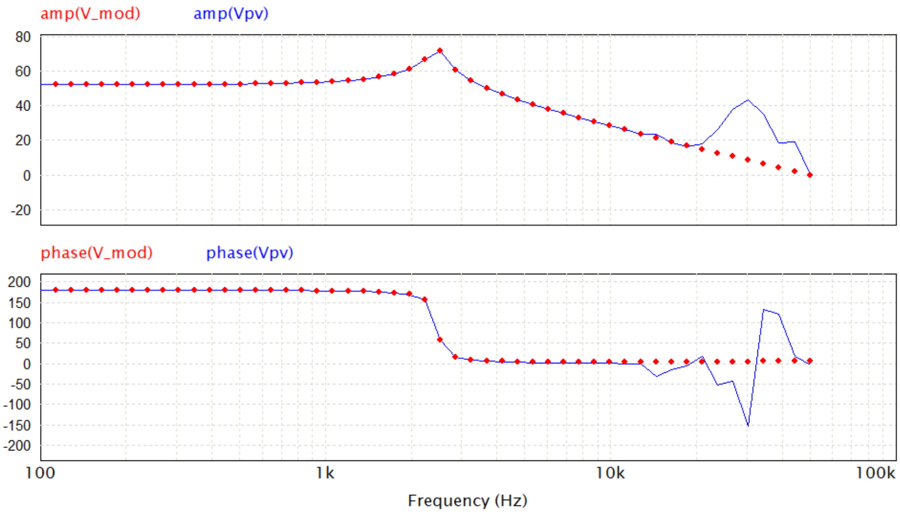

Figure 11. Comparison of the frequency responses of the Norton model and the PSIM circuit in the Boost mode for PV voltage V_{pv}. [●: mathematical model results. —: circuital simulation results].

From Figure 11 it can be concluded that the small-signal analytical model accurately describes the dynamics of the system operating in the boost mode up to approximately 12 kHz for the variable V_{pv}; therefore, it is suitable for control purposes.

2.6. Control Design

In this section, the controller design will be explained in detail. The control technique used for the proposed converter topology is based on pulse width modulation (PWM) by operating with a constant switching frequency [45]. A traditional proportional integral (PI) controller is designed for both modes of operation, i.e., boost mode and buck mode. However, for the buck operation mode a current controller for inductor current $I_L(s)$ is designed, and for the boost operation mode a voltage controller for PV voltage V_{pv} to optimize a perturb and observe (P&O) MPPT is designed [44,52].

2.6.1. Buck Operation Mode

In this mode of operation, a PI current controller with a single negative feedback loop structure was designed to regulate inductor current $I_L(s)$ by using a reference value defined. In this case, it is regulated to the current at the MPP of the solar PV panel. The block diagram of the current controller is shown in Figure 12.

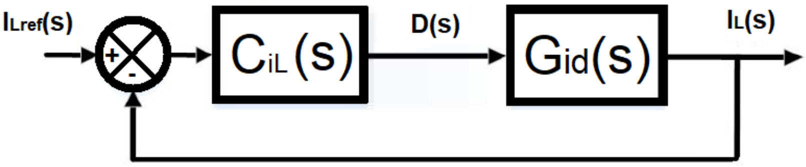

Figure 12. Block diagram of the current controller for the proposed converter operating in the Buck mode.

The PI controller was tuned using the MATLAB SISO tool by adding a real zero, and integrator to meet the desired dynamic behavior of the system. The PI controller was required to have a negative sign to compensate for the negative sign of the $G_id(s)$ transfer function. A damping ratio equal to or higher to 0.707 was defined, as well as a crossover frequency of 12 kHz with a gain margin of −3 dB according to the AC sweep results analyzed before. Satisfying the aforementioned design parameters, the controller coefficients obtained are:

$$K_p = -0.2753; T_n = 4.5351 \times 10^{-5} \tag{24}$$

2.6.2. Boost Operation Mode

In the boost operation mode, a PI voltage controller with a single negative feedback loop structure was designed to regulate the PV voltage $V_{PV}(s)$ using a reference value defined by a P&O MPPT. Therefore, in the boost mode, the converter provides the maximum power to the load, keeping a constant voltage at the input. The block diagram of the voltage controller with MPPT is shown in Figure 13.

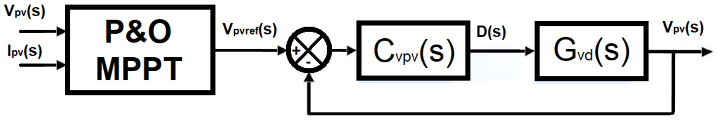

Figure 13. Block diagram of the voltage controller with MPPT for the proposed converter operating in the Boost mode.

The design parameters established are the same as those mentioned in the design of the PI buck controller. However, it was not possible to comply with the damping ratio design requirement, giving as a result a high underdamped response. Nevertheless, the other aforementioned design parameters were satisfied, obtaining the controller coefficients defined as follows:

$$K_p = -0.025015; T_n = 7.5758 \times 10^{-4} \tag{25}$$

2.6.3. Power Management

A power management system will control the two separate buck and boost mode controllers through a power management command [53], as shown in Figure 14. A switch connected between both modes of operation will be operated according to a control algorithm flowchart shown in Figure 15.

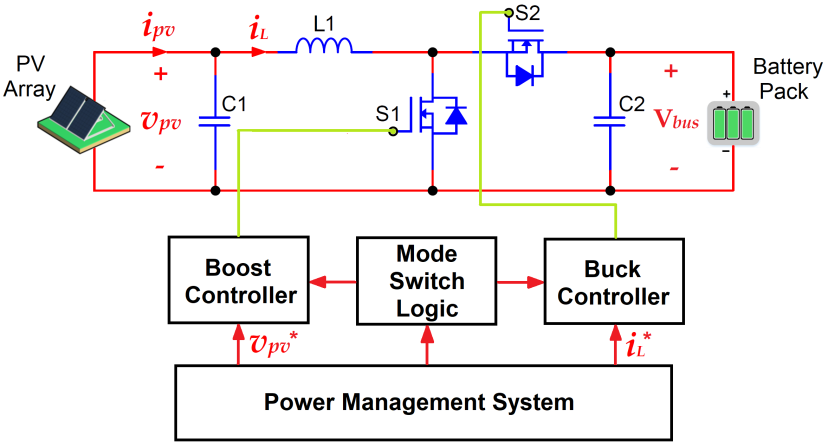

Figure 14. Circuit diagram of power management control.

In the control algorithm flowchart shown in Figure 15, it can be noted that only when the EV battery pack is connected to the system and the power provided by the solar PV array is higher than 1000 W, will the EV battery pack will be fed by the solar PV array (boost operation mode). Otherwise, a main storage or the grid will feed the solar PV array through a second bidirectional converter as shown before in Figure 5. However, when an EV battery pack is not connected to the system and the weather conditions meet the parameters (temperature below zero/snowing/freezing rain), then the buck mode will go into operation.

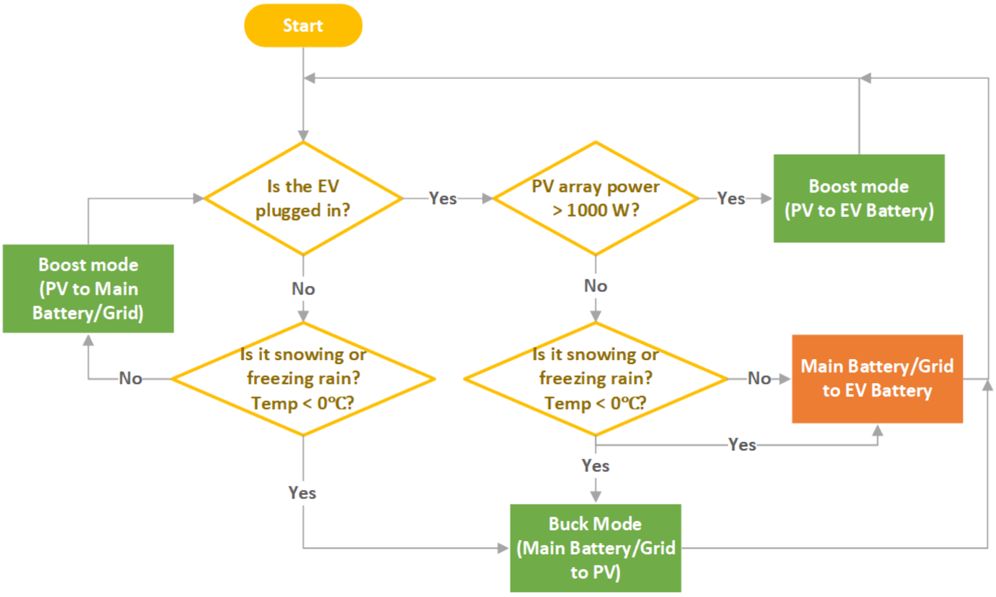

Figure 15. Control algorithm flowchart.

If the weather condition parameters (temperature below zero/snowing/freezing rain) are not met, the solar PV array will feed the main battery or the grid, depending on the system configuration.

3. Simulation Results

This section shows the simulation results for the different operating modes of proposed converter control.

3.1. Buck Operation Mode

The controller designed for the buck operation mode was simulated using PSIM software. For control and simulation purposes the PV solar array was assumed as a load resistance. The circuit diagram is shown in Figure 16. The performance of the control was evaluated in terms of its capacity to reject perturbances in the inductor current reference, the bus voltage and the load.

The validation test applied in this mode of operation consisted of forcing the steady state of the converter by regulating the inductor current I_L and therefore the PV current I_{pv} to 8.13 A with a PV voltage V_{pv} of 271.8 V. Then, at 6 ms a negative step was applied to the inductor current reference to validate the robustness of the system, changing from 8.13 A to 7.13 A. After that, a disturbance in the bus voltage V_{bus} was applied, where the EV battery pack is connected, at 10 ms setting a change of 5 V, from 400 V to 405 V. Finally, a change on the load was set at 14 ms, decreasing the load from 33.43 Ω to 30.47 Ω.

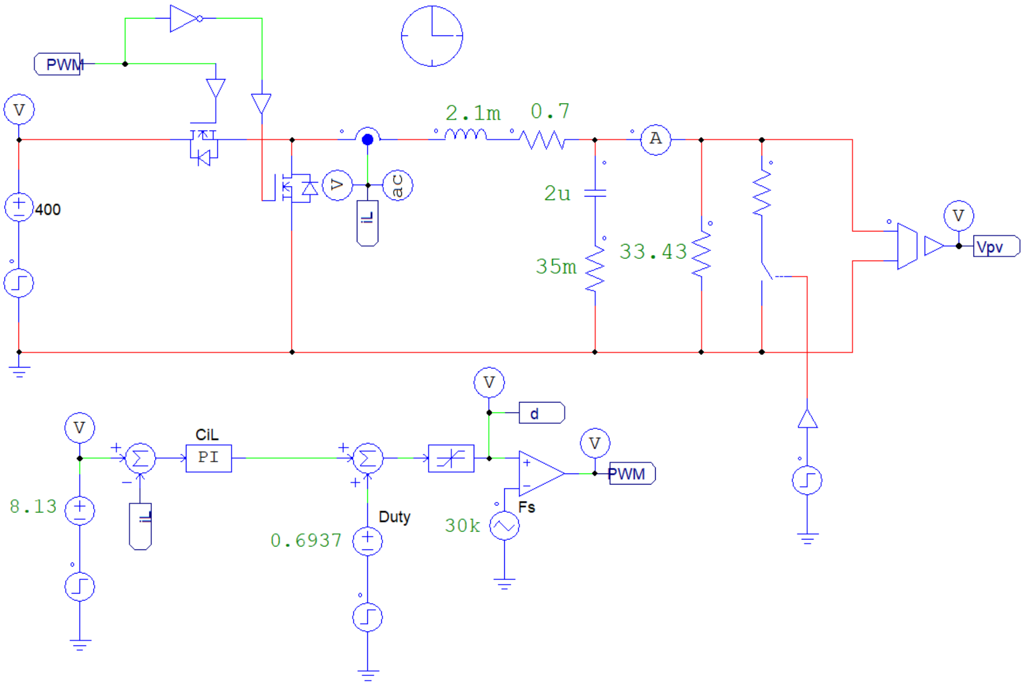

Figure 16. Circuit diagram for the current controller in the Buck mode.

Figure 17 shows the simulated waveforms for all the cases aforementioned. The first waveform shows the inductor current I_L, the solar PV array current I_{PV} and control reference current I_{Lref}. The second waveform depicts the PV array voltage V_{PV}, while the third waveform shows the bus voltage V_{bus}. Finally, the last waveform shows the duty cycle applied to the controller.

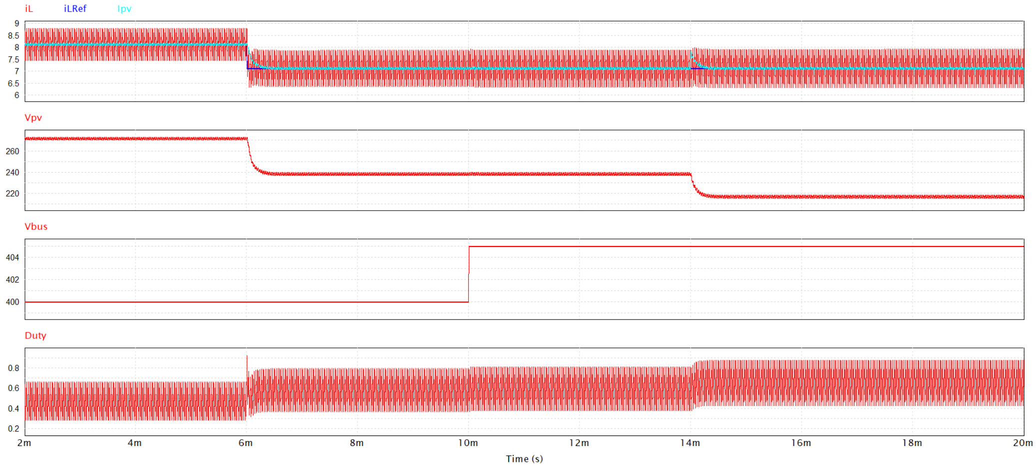

Figure 17. Performance analysis for different perturbances in the Buck mode.

As can be seen in Figure 17, the proposed control accurately rejected all disturbances, showing a settling time below 0.1 ms with little noticeable deviation voltage. In all cases, the current was regulated uniformly to the set reference point which was 7.13 A, despite applied disturbances.

3.2. Boost Operating Mode

In the boost operating mode, the P&O MPPT with the voltage controller applied to the proposed converter was simulated to validate the close-loop behaviour of the system under different irradiance conditions.

Figure 18 shows the circuit diagram for the final boost mode controller. For this simulation a PSIM PV model was applied, using the parameters given in Table 1. The behaviour of the system was evaluated by changing the irradiance conditions of the solar PV array, maintaining a constant temperature.

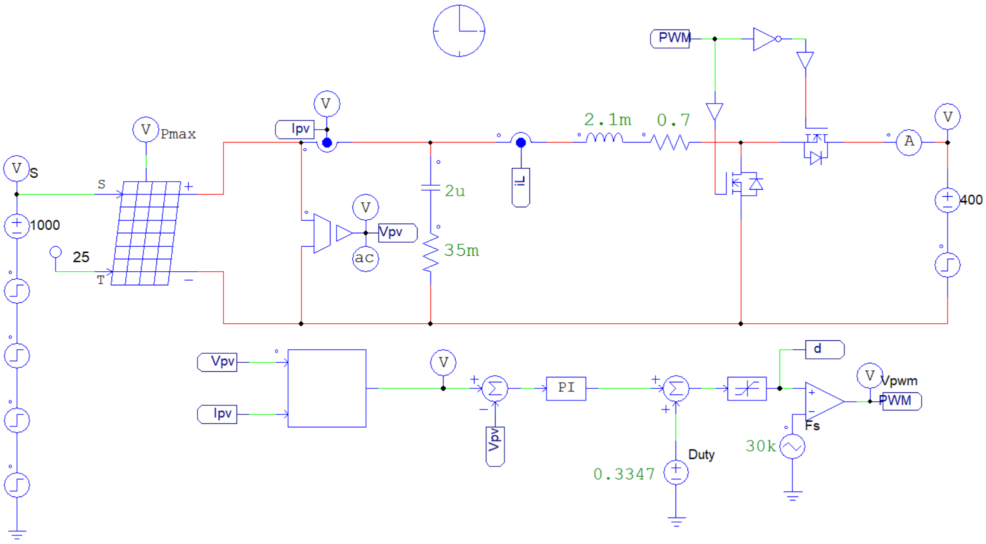

Figure 18. Circuit diagram for the P&O MPPT with the voltage controller in Boost mode.

Figure 19 shows the simulation results that validate the response of the proposed converter in steady state. The P&O MPPT developed is a digital control that looks for the MPP by changing the voltage reference every 0.35 ms. The control increases or decreases the voltage in steps of 250 mV depending on the measured power of the PV array and when the stable condition is reached the algorithm oscillates around the peak power point as can be seen in the first waveform of the solar PV voltage (V_{pv}) and in the third waveform of the solar PV power ($V_{pv} \times I_{pv}$) in Figure 19.

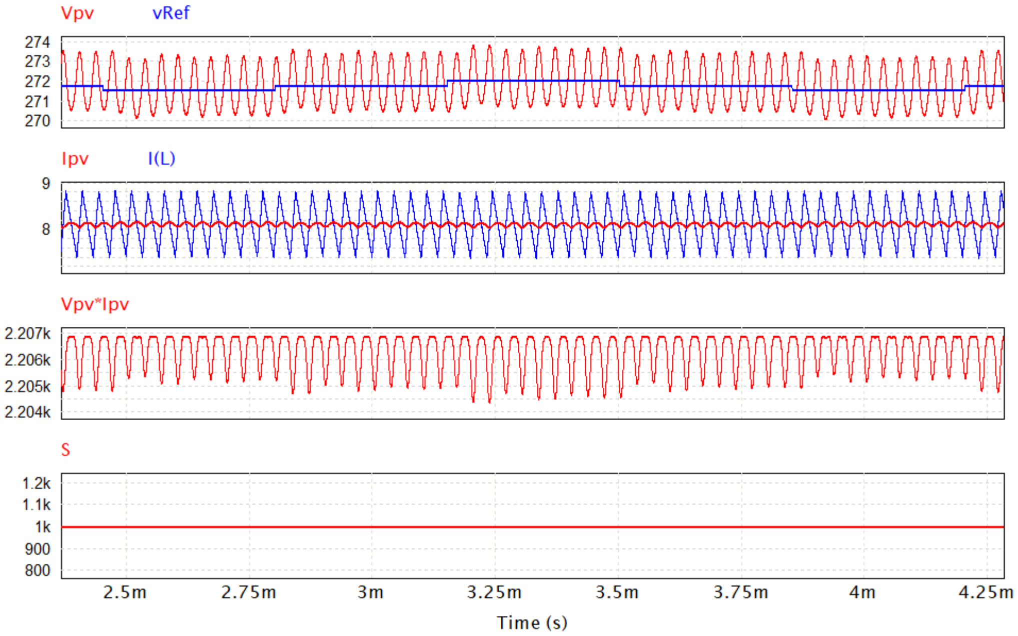

Figure 19. Simulated waveforms during the validation test of the P&O MPPT with the voltage controller for an irradiance of 1000 W/m^2 in the Boost mode.

The profile of irradiation used to validate the operation of the proposed converter in boost mode was set to force a steady state at the maximum power point of the converter, by starting with an irradiance of 1000 W/m^2 for time 2–6 ms; after that the irradiance was changed by introducing negative steps of 4 ms resulting in the following values: 900 W/m^2 for time 6–10 ms, 800 W/m^2 for time 10–14 ms, 400 W/m^2 for time 14–18 ms and finally a positive step, resulting in an irradiance of 1000 W/m^2 for time 18–20 ms. Temperature was kept constant at 25 °C throughout the simulation. The profile of irradiation is depicted in the waveform shown in Figure 20.

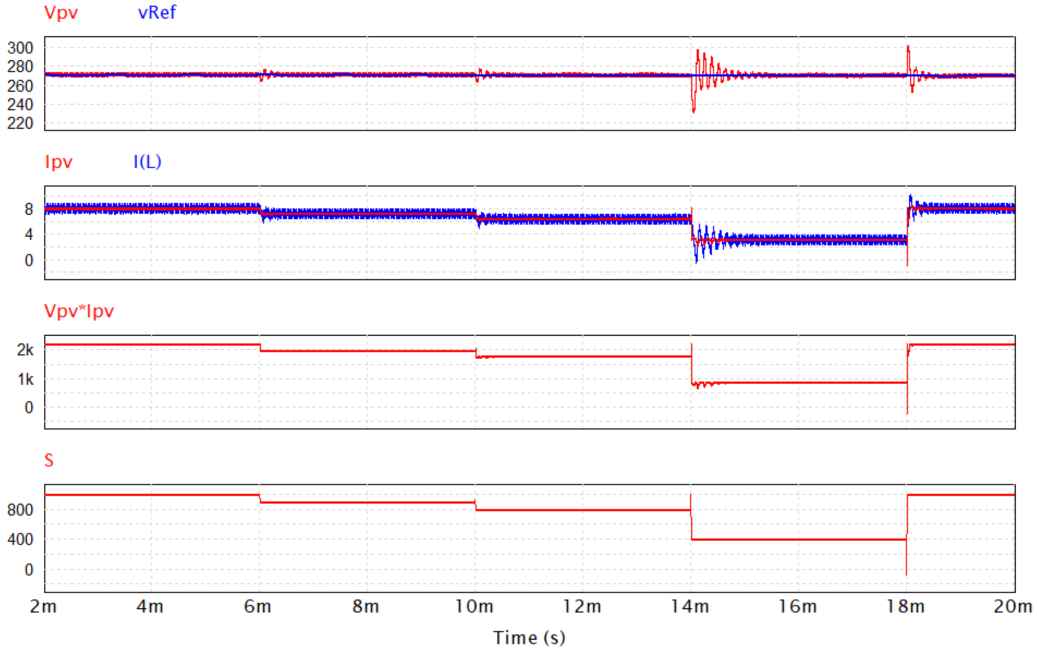

Figure 20. Simulated waveforms during the validation test of the P&O MPPT with the voltage controller for different irradiances in Boost mode.

In Figure 20, the transient response of a negative step change of 100 W/m^2 (from 1000 to 900 W/m^2) in the irradiance can be seen at 6 ms. The waveforms show a rejection of the perturbation with a voltage deviation below 6.58 V (2.42%) and a settling time of about 0.17 ms to recover to the steady state. At 10 ms the waveforms show a similar transient response. Once more, a negative step change of 100 W/m^2 (from 900 to 800 W/m^2) was applied in the irradiance. In this case, the waveforms show a rejection of the perturbance producing a voltage deviation below 6.94 V (2.55%) and a settling time of about 0.17 ms to recover to steady state. It can be noted that when the power of the PV array is close to the MPP, the control rejects the perturbances producing a smaller overshoot peak voltage than when the PV array power is getting away of the MPP.

On the other hand, at 14 ms there was an abrupt decrease of 400 W/m^2 (from 800 to 400 W/m^2) in the irradiance; the proposed control rejected this perturbation producing a voltage deviation below 14.7% (39.55 V) and showed a settling time of about 0.73 ms to recover the steady state. Finally, at 18 ms, when there was a sharp increase in the irradiance of 600 W/m^2 (from 400 to 1000 W/m^2), the proposed control again rejected the perturbance with voltage deviations below 31.71 V (11.7%) and showed a faster settling time of about 0.26 ms to recover the steady state.

It is worth mentioning that the system transient response when there is an abrupt increase in irradiance disturbances shows a faster recovery and a lower overshoot peak voltage when approaching the maximum power point of the PV array, than when the system is exposed to an abrupt decrease in irradiance, moving away from the maximum power point.

4. Conclusions

This paper presents a detailed review of the effects and solutions used to improve the efficiency of solar PV systems in extreme winter conditions (snow cover). However, sufficient electrical solutions have not been fully explored among academic researchers, and as a result, the academic literature is insufficient. Therefore, a bidirectional DC-DC buck-boost converter—also called synchronous buck converter—is proposed to meet these needs in EV charging applications.

The design and simulations evidenced satisfactorily the fulfillment of the functions of the proposed converter: providing a regulated current in the direction to the PV array that will produce heat in the PV cells to melt the snow cover from the solar panels; and providing maximum power to charge the EV battery pack. The regulated current selected in the buck mode of operation was equal to the MPP current of the solar PV module, 8.13 A. In the case of the boost mode of operation, the P&O MPPT regulated the power of the converter at 2.2 kW regardless of the disturbances applied to the system.

The proposed control provides a robust dynamic response to different disturbances in both modes of operation, buck and boost, as demonstrated by the simulations.

Author Contributions: Conceptualization, S.A.-A. and S.S.W.; methodology, S.A.-A. and A.H.K.; writing the original draft preparation, S.A.-A.; reviewed and edited the final draft, S.A.-A., A.H.K., T.S. and S.S.W.; supervision, S.S.W.; funding acquisition, S.S.W. and T.S. All authors have read and agreed to the published version of the manuscript.

Funding: This research was funded by the Canada Research Chairs (CRC) Program and The Natural Sciences and Engineering Research Council of Canada (NSERC).

Institutional Review Board Statement: Not applicable.

Informed Consent Statement: Not applicable.

Data Availability Statement: Not applicable.

Acknowledgments: The authors would like to acknowledge the technical guidance and support from all past and current research personnel at the Ontario Tech University's -Smart Transportation Electrification and Energy Research (STEER) group. We also would like to acknowledge the support from Rick Szymczyk, Sherif Abdelsamad, and the Upstartz Energy Ltd. for the equipment provided for experimentation.

Conflicts of Interest: The authors declare no conflict of interest.

References

1. Rahmatmand, A. Experimental and Numerical Investigation of Snow Removal from Photovoltaic Solar Panels. Doctoral Dissertation, Queen's University, Kingston, ON, Canada, 2018.
2. REN21. *Renewables 2010 Global Status Report*; Technical Report; REN21 Secretariat: Paris, France, 2010.
3. Ueda, Y.; Kurokawa, K.; Itou, T.; Kitamura, K.; Miyamoto, Y.; Yokota, M.; Sugihara, H. Performance Ratio and Yield Analysis of Grid Connected Clustered PV Systems in Japan. In Proceedings of the 2006 IEEE 4th World Conference on Photovoltaic Energy Conference, Waikoloa, HI, USA, 7–12 May 2006; pp. 2296–2299.
4. Klugmann-Radziemska, E. Shading, Dusting and Incorrect Positioning of Photovoltaic Modules as Important Factors in Performance Reduction. *Energies* **2020**, *13*, 1992. [CrossRef]
5. Sathyanarayana, P.; Ballal, R.; Sagar, P.L.; Kumar, G. Effect of shading on the performance of solar PV panel. *Energy Power* **2015**, *5*, 1–4.
6. Tabanjat, A.; Becherif, M.; Hissel, D. Reconfiguration solution for shaded PV panels using switching control. *Renew. Energy* **2015**, *82*, 4–13. [CrossRef]
7. Potnuru, S.R.; Pattabiraman, D.; Ganesan, S.I.; Chilakapati, N. Positioning of PV panels for reduction in line losses and mismatch losses in PV array. *Renew. Energy* **2015**, *78*, 264–275. [CrossRef]
8. Patel, H.; Agarwal, V. MATLAB-based modeling to study the effects of partial shading on PV array characteristics. *IEEE Trans. Energy Convers.* **2008**, *23*, 302–310. [CrossRef]
9. Alsayid, B.; Alsadi, S.; Jallad, J.; Dreidy, M. Partial shading of PV system simulation with experimental results. *Smart Grid Renew. Energy* **2013**, *4*, 429–435. [CrossRef]
10. Fouad, M.; Shihata, L.A.; Morgan, E.I. An integrated review of factors influencing the performance of photovoltaic panels. *Renew. Sustain. Energy Rev.* **2017**, *80*, 1499–1511. [CrossRef]

11. Taghvaee, M.; Radzi, M.; Moosavain, S.; Hizam, H.; Hamiruce Marhaban, M. A current and future study on non-isolated DC–DC converters for photovoltaic applications. *Renew. Sustain. Energy Rev.* **2013**, *17*, 216–227. [CrossRef]
12. Kjaer, S.B.; Pedersen, J.K.; Blaabjerg, F. A review of single-phase grid-connected inverters for photovoltaic modules. *IEEE Trans. Ind. Appl.* **2005**, *41*, 1292–1306. [CrossRef]
13. Lohner, A.; Meyer, T.; Nagel, A. A new panel-integratable inverter concept for grid-connected photovoltaic systems. In Proceedings of the IEEE International Symposium on Industrial Electronics, Warsaw, Poland, 17 June 1996; Volume 2, pp. 827–831.
14. Papanikolaou, N.P.; Tatakis, E.C.; Critsis, A.; Klimis, D. Simplified high frequency converter in decentralized grid-connected PV systems: A novel low-cost solution. In Proceedings of the Electric Power Engineering Conference, Toulouse, France, 2–4 September 2003.
15. Powers, L.; Newmiller, J.; Townsend, T. Measuring and modeling the effect of snow on photovoltaic system performance. In Proceedings of the 2010 35th IEEE Photovoltaic Specialists Conference, Honolulu, HI, USA, 20–25 June 2010; pp. 000973–000978.
16. Becker, G.; Schiebelsberger, B.; Weber, W. An Approach to the Impact of Snow on the Yield of Grid Connected PV Systems. In Proceedings of the 21st European Photovoltaic Solar Energy Conference and Exhibition, Dresden, Germany, 4–8 September 2006; p. 4.
17. Nakagawa, S.; Tokoro, T.; Nakano, T.; Hayama, K.; Ohyama, H.; Yamaguchi, T. An effect of snow for electric energy generation by 40 kW PV system. In Proceedings of the 3rd World Conference on Photovoltaic Energy Conversion, Osaka, Japan, 11–18 May 2003; p. 4.
18. Andrews, R.W.; Pearce, J.M. The effect of spectral albedo on amorphous silicon and crystalline silicon solar photovoltaic device performance. *Sol. Energy* **2013**, *91*, 233–241. [CrossRef]
19. Andrews, R.W.; Pearce, J.M. Prediction of energy effects on photovoltaic systems due to snowfall events. In Proceedings of the 2012 38th IEEE Photovoltaic Specialists Conference, Austin, TX, USA, 3–8 June 2012; pp. 003386–003391.
20. Andrews, R.W.; Pollard, A.; Pearce, J.M. A new method to determine the effects of hydrodynamic surface coatings on the snow shedding effectiveness of solar photovoltaic modules. *Sol. Energy Mater. Sol. Cells* **2013**, *113*, 71–78. [CrossRef]
21. Awad, H.; Gül, M.; Salim, K.; Yu, H. Predicting the energy production by solar photovoltaic systems in cold-climate regions. *Int. J. Sustain. Energy* **2018**, *37*, 978–998. [CrossRef]
22. Brench, B. *Snow-Covering Effects on the Power Output of Solar Photovoltaic Arrays*; Technical Report COO–4094-61, 5232456; The U.S. Department of Energy: Lexington, MA, USA, 1979.
23. Heidari, N.; Gwamuri, J.; Townsend, T.; Pearce, J.M. Impact of Snow and Ground Interference on Photovoltaic Electric System Performance. *IEEE J. Photovoltaics* **2015**, *5*, 1680–1685. [CrossRef]
24. Marion, B.; Rodriguez, J.; Pruett, J. *Instrumentation for Evaluating PV System Performance Losses from Snow: Preprint*; American Solar Energy Society (ASES): Buffalo, NY, USA, 2009; p. 9.
25. Marion, B.; Schaefer, R.; Caine, H.; Sanchez, G. Measured and modeled photovoltaic system energy losses from snow for Colorado and Wisconsin locations. *Sol. Energy* **2013**, *97*, 112–121. [CrossRef]
26. Pawluk, R.E. Observations of Snow and Ice Formation on Solar Photovoltaic Panels and an Enhanced Method of Modelling Snow Melting from Solar Photovoltaic Panels. Master's Dissertation, University of Alberta, Edmonton, Alberta, 2019.
27. Pawluk, R.E.; Chen, Y.; She, Y. Photovoltaic electricity generation loss due to snow—A literature review on influence factors, estimation, and mitigation. *Renew. Sustain. Energy Rev.* **2019**, *107*, 171–182. [CrossRef]
28. Riley, D.; Burnham, L.; Walker, B.; Pearce, J.M. Differences in Snow Shedding in Photovoltaic Systems with Framed and Frameless Modules. In Proceedings of the 2019 IEEE 46th Photovoltaic Specialists Conference (PVSC), Chicago, IL, USA, 16–21 June 2019; pp. 558–561.
29. Becker, G.; Schiebelsberger, B.; Weber, W.; Schumacher, J.; Zehner, M.; Wotruba, G.; Vodermayer, C. Energy Yields of PV Systems—Comparison of Simulation and Reality. In Proceedings of the 23rd European Photovoltaic Solar Energy Conference and Exhibition, Valencia, Spain, 1–5 September 2008; pp. 3184–3186.
30. Jelle, B.P. The challenge of removing snow downfall on photovoltaic solar cell roofs in order to maximize solar energy efficiency—Research opportunities for the future. *Energy Build.* **2013**, *67*, 334–351. [CrossRef]
31. Brearley, D. Designing PV systems for environmental extremes. *SolarPro* **2015**, *8*, 54–70.
32. Andenæs, E.; Jelle, B.P.; Ramlo, K.; Kolås, T.; Selj, J.; Foss, S.E. The influence of snow and ice coverage on the energy generation from photovoltaic solar cells. *Sol. Energy* **2018**, *159*, 318–328. [CrossRef]
33. Ross, M.; Usher, E. Photovoltaic Array Icing and Snow Accumulation: A Study of a Passive Melting Technology. In Proceedings of the 21st Annual Conference of the Solar Energy Society of Canada, Toronto, ON, Canada, 31 October–2 November 1995; Volume 31, pp. 21–26.
34. Ross, M. *Snow and Ice Accumulation on Photovoltaic Arrays: An Assessment of the TN Conseil Passive Melting Technology*; Technical Report EDRL 95-68 (TR); Energy Diversification Research Laboratory, CANMET, Natural Resources Canada: Varennes, France, 1995.
35. Innos. Weight Watcher—Innos. Available online: https://www.innos.no/weight-watcher/ (accessed on 6 January 2021).
36. Laurent Aubert, Martigny. Les Panneaux Solaires qui Défient la Neige, 2014. Available online: https://www.24heures.ch/suisse/suisse-romande/panneaux-solaires-defient-neige/story/20491743 (accessed on 6 January 2021).
37. Weiss, A.; Weiss, H. Photovoltaic cell electrical heating system for removing snow on panel including verification. *Environ. Sci. Pollut. Res.* **2018**, *25*, 24561–24568. [CrossRef] [PubMed]

38. Asthana, D.; Zinaddinov, M.; Ushakov, M.; Mil'shtein, S. Cost-Effective Snow Removal from Solar Panels. In Proceedings of the IEEE 46th Photovoltaic Specialists Conference (PVSC), Chicago, IL, USA, 16–21 June 2019; pp. 1312–1315.
39. Van Straten, G.A. Heated Solar Panel System and Method. U.S. Patent 20150021310, 22 January 2015.
40. Husu, A.G.; Stan, M.F.; Cobianu, C.; Fidel, N.; Nedelcu, O. An inedited solution to increase the energy efficiency of photovoltaic panels for regions with snow. In Proceedings of the 13th International Conference on Engineering of Modern Electric Systems (EMES), Oradea, Romania, 11–12 June 2015; pp. 1–4.
41. Jelle, B.P.; Gao, T.; Mofid, S.A.; Kolås, T.; Stenstad, P.M.; Ng, S. Avoiding Snow and Ice Formation on Exterior Solar Cell Surfaces – A Review of Research Pathways and Opportunities. *Procedia Eng.* **2016**, *145*, 699–706. [CrossRef]
42. Rahmatmand, A.; Harrison, S.J.; Oosthuizen, P.H. An experimental investigation of snow removal from photovoltaic solar panels by electrical heating. *Sol. Energy* **2018**, *171*, 811–826. [CrossRef]
43. Petrone, G.; Ramos-Paja, C.A.; Spagnuolo, G. *Photovoltaic Sources Modeling*; John Wiley & Sons Ltd.: Hoboken, NJ, USA, 2017.
44. Paja, R.; Andres, C. Modelado de un Sistema Fotovoltaico. 2020. Available online: https://www.youtube.com/watch?v=NlIk3gf36EA (accessed on 22 December 2021).
45. López-Santos, O.; Aldana-Rodríguez, Y.A.; Garcia, G.; Martínez-Salamero, L. A Unified Multimode Control of a DC–DC Interlinking Converter Integrated into a Hybrid Microgrid. *Electronics* **2019**, *8*, 1314. [CrossRef]
46. Lozano Nieto, J.M. Diseño y Simulación de un Regulador de Histéresis con Frecuencia de Conmutación Fija. Ph.D. Thesis, Universitat Politecnica de Catalunya, Barcelona, Spain, 2007.
47. Chao, K.H.; Tseng, M.C.; Huang, C.H.; Liu, Y.G.; Huang, L.C. Design and Implementation of a Bidirectional DC-DC Converter for Stand-Alone Photovoltaic Systems. *Int. J. Comput. Consum. Control. (IJ3C)* **2013**, *2*, 12.
48. Texas Instruments. *Basic Calculation of a Boost Converter's Power Stage*; Application Report SLVA372C; Texas Instruments: Dallas, TX, USA, 2009.
49. Texas Instruments. *Basic Calculation of a Buck Converter's Power Stage*; Application Report SLVA477B; Texas Instruments: Dallas, TX, USA, 2011.
50. Gonzalez, D.; Ramos-Paja, C.A.; Petrone, G. Automated Procedure for Calculating the Controller Parameters in Photovoltaic DC/DC Converters. *Int. Rev. Electr. Eng.* **2011**, *6*, 14.
51. Ugur, E.; Vural, B. Comparison of different small signal modeling methods for bidirectional DC-DC converter. In Proceedings of the 2014 International Conference on Renewable Energy Research and Application (ICRERA), Milwaukee, WI, USA, 19–22 October 2014; pp. 913–915.
52. Femia, N.; Petrone, G.; Spagnuolo, G.; Vitelli, M. Optimization of Perturb and Observe Maximum Power Point Tracking Method. *IEEE Trans. Power Electron.* **2005**, *20*, 963–973. [CrossRef]
53. Zhang, J.; Lai, J.-S.; Yu, W. Bidirectional DC-DC converter modeling and unified controller with digital implementation. In Proceedings of the Twenty-Third Annual IEEE Applied Power Electronics Conference and Exposition, Austin, TX, USA, 24–28 February 2008; pp. 1747–1753.